

Extremely Confined Acoustic Phonon Polaritons in Monolayer-hBN/
Metal Heterostructures for Strong Light–Matter InteractionsZhu Yuan,[†] Runkun Chen,[†] Peining Li,^{*} Alexey Y. Nikitin, Rainer Hillenbrand, and Xinliang Zhang^{*}Cite This: *ACS Photonics* 2020, 7, 2610–2617

Read Online

ACCESS |



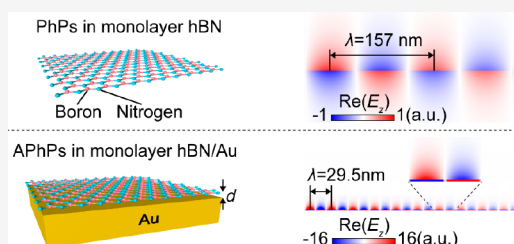
Metrics & More



Article Recommendations

ABSTRACT: Phonon polaritons in polar van der Waals materials enable strong electromagnetic-field confinement and enhancement for deeply subwavelength scale light-matter interactions. Here we propose and theoretically study acoustic phonon polaritons (APhPs) supported by a monolayer of hexagonal boron nitride (hBN) located at a few nanometers distance above a metal substrate. Compared to conventional hBN phonon polaritons, APhPs exhibit much larger polariton confinement, stronger near-field enhancement, and slower group velocity, altogether with nearly identical polariton lifetimes. These remarkable properties allow APhP-based nano-resonators to significantly enhance vibrational fingerprints of subnanometer-thick molecule layers, achieving strong coupling between molecular vibrations and APhP modes. Our work demonstrates the great potential of APhPs for exploring strong light–matter interactions at an extremely deep subwavelength-scale.

KEYWORDS: hexagonal boron nitride, monolayer, phonon polariton, extreme confinement, strong light–matter interaction, surface-enhanced infrared absorption spectroscopy



Phonon polaritons, hybridized states of infrared photons and optical phonons (lattice vibrations) in polar van der Waals (vdW) materials, have attracted great attention due to their strong electromagnetic-field confinement,^{1,2} ultraslow group velocities,^{3,4} long lifetimes,^{1,5,6} and extreme polariton anisotropy (hyperbolic dispersion).^{1,7–10} Relevant applications include high-quality nanoresonators,^{11–13} super-resolution imaging,^{7,8} field-enhanced molecular sensing,^{14,15} subdiffraction waveguiding,^{8,16} infrared metasurfaces,^{9,17–20} the enhancement of single photon emission and extraction,²¹ and many others.²² Atomically thin layers of high-quality polar vdW materials can be obtained by mechanical exfoliation techniques,^{23,24} which allow for tuning the confinement of phonon polaritons by changing the layer thickness with atomic-layer precision.^{5,25} Ultimately, it has been experimentally shown that the confinement of phonon polaritons can approach $\lambda_0/\lambda_p = 60$ (λ_p and λ_0 being the wavelengths of phonon polaritons and free-space photons, respectively) when the flake of vdW materials reduces to a one-atomic layer.²⁵ However, as the vdW materials cannot be thinner than a one-atomic layer, a further increase of the polariton confinement is thus limited.

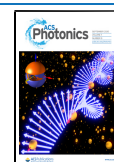
To overcome this limitation, here we propose and investigate a new type of phonon polariton, acoustic phonon polaritons (APhPs) that are supported by a monolayer of hexagonal boron nitride (hBN, a prototypical polar vdW material) placed above a metallic substrate (e.g., Au) with a separation distance d (Figure 1a, bottom). Analogously to acoustic graphene plasmons in graphene/metal heterostruc-

tures,^{26–32} the APhPs originate from the hybridization of phonon polaritons (PhPs) in the hBN monolayer and their electromagnetic “mirror image” in the metal. Such a hybridization strongly squeezes the electromagnetic field of APhPs into the nanoscale gap between the hBN layer and the metal. Consequently, both the vertical and lateral confinement of APhPs are significantly increased as compared to the PhPs in the hBN monolayer (see Figure 1b). By reducing the width of the gap, extreme confinement (surpassing the diffraction limit by orders of magnitude) of electromagnetic fields of APhPs can be achieved. Although hyperbolic volume phonon polariton modes in thick hBN layers on the metallic substrate have been investigated,^{33–38} APhPs in monolayer-hBN/metal heterostructures have been explored neither experimentally nor theoretically.

To demonstrate the extreme confinement of APhPs, we numerically simulate the electric field distribution of the APhPs in the hBN/Au heterostructures using the commercial software package COMSOL. In the simulations, the hBN monolayer is modeled as a two-dimensional conducting sheet with an effective conductivity^{10,25} given by $\sigma_{\text{eff}} \approx -i\omega\hbar\epsilon_0\epsilon_{\text{hBN},L}$, with

Received: June 18, 2020

Published: July 31, 2020



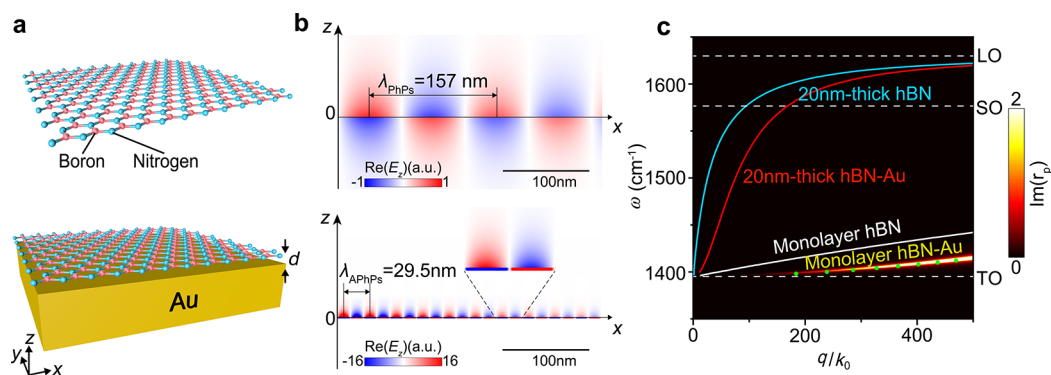


Figure 1. Electric field distribution and dispersion of APhPs and PhPs. (a) Schematics for monolayer hBN (upper panel) and monolayer hBN separated from the Au substrate by a gap width of d (lower panel). (b) Electric field distribution $\text{Re}(E_z)$ of hBN monolayer PhPs (upper panel) and APhPs ($d = 0.5$ nm, lower panel) at $\omega = 1400$ cm^{-1} (free-space wavelength $\lambda_0 = 7.1$ μm). The inset provides an enlarged view to the field distribution. The wavelengths of the PhPs and APhPs are indicated by horizontal arrows. (c) Dispersion relations of APhPs with a gap width $d = 0.5$ nm (false color image shows the imaginary part of the calculated Fresnel reflection coefficient; green dots show results obtained with a numerical mode solver), PhPs on isolated monolayer hBN (white line), APhPs on a 20 nm thick hBN layer at a distance of 0.5 nm to the Au substrate (red line), and PhPs on a 20 nm thick isolated hBN layer (blue line). Dashed white lines mark the LO (longitudinal optical phonon), SO (surface optical phonon), and TO (transverse optical phonon) frequency of hBN, respectively.

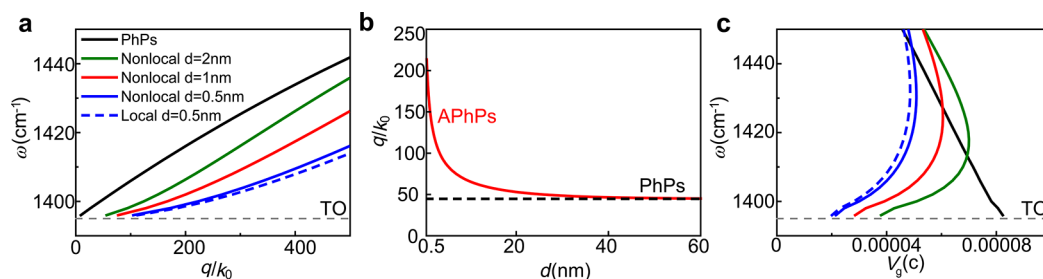


Figure 2. Nonlocality and gap-width tuning of dispersion and group velocity of hBN monolayer APhPs. (a) Dispersion of APhPs for three different gap widths, $d = 2$ nm (solid green line), $d = 1$ nm (solid red line), and $d = 0.5$ nm (solid blue line), which are calculated by considering that a nonlocal metal is below the monolayer hBN. Solid black line shows dispersion of PhPs on isolated hBN monolayer. (b) Gap-width-dependent wave vector of APhPs (considering nonlocal Au), q , normalized to free-space wavevector k_0 (red line). Dashed black line shows normalized wavevector of hBN monolayer PhPs. (c) Calculated group velocities of APhPs ($d = 2$ nm, solid green line; $d = 1$ nm, solid red line; $d = 0.5$ nm, solid blue line) and PhPs (solid black line) by considering a nonlocal Au below the monolayer hBN. Dashed gray lines in (a) and (c) mark the TO (transverse optical phonon) frequency of hBN. Dashed blue lines in (a) and (c) show the results of APhPs for the hBN layer on the local Au ($d = 0.5$ nm), which are slightly different from the results obtained for nonlocal Au.

the thickness of the monolayer $h = 0.34$ nm and $\epsilon_{\text{hBN},\perp}$ being the in-plane permittivity of bulk hBN crystals. Note that the in-plane permittivity $\epsilon_{\text{hBN},\perp}$ of bulk crystals can be used for approximately describing the properties of PhPs in hBN monolayers according to recent experimental and theoretical studies.^{25,39,40} Figure 1b shows the simulated electric field distribution $\text{Re}(E_z)$ of APhPs and PhPs in a free-standing hBN monolayer at the frequency of 1400 cm^{-1} (free-space wavelength $\lambda_0 = 7.1$ μm), respectively. One can observe that the electric field of PhPs exhibits a vertical symmetry at both sides of hBN, while the APhPs have a vertically asymmetrical electric field distribution and especially exhibit a strong capacitor-like (squeezed) electric field in the gap ($d = 0.5$ nm). Owing to the strong field squeezing, the maximum near-field enhancement (found in the gap) of APhPs is $16\times$ larger than that of the PhPs. Importantly, the wavelength of APhPs ($\lambda_p = 29.5$ nm, $\lambda_0/\lambda_p = 242$) is also much shorter than that of PhPs ($\lambda_p = 157$ nm, $\lambda_0/\lambda_p = 45$), confirming the significantly enhanced polariton confinement.

We further explore theoretically the dispersion of APhPs by calculating the Fresnel reflection coefficient $r_p(q, \omega)$ of the hBN/Au heterostructure. We focus on propagating APhPs in the upper Reststrahlen band (1395 – 1630 cm^{-1}) of hBN,

because hBN phonon polaritons in the lower Reststrahlen band (785 – 845 cm^{-1}) usually exhibit a shorter propagation length.³ The obtained result is plotted as a false-color map in Figure 1c, where the APhP modes are manifested by a maximum reflection⁶ (indicated by yellow color). We also perform simulations by using the mode solver of COMSOL to obtain the dispersion of the propagating APhP modes (green dots), which shows an excellent agreement with the dispersion obtained from the Fresnel reflection coefficient r_p . For comparison, we also plot in Figure 1c the dispersion of PhPs in monolayer hBN, as well as the dispersion of the fundamental phonon polariton waveguide modes in a 20 nm thick hBN layer and in a hBN (20 nm thick)/Au heterostructure (gap width = 0.5 nm), respectively (all are calculated by the mode solver). We see that the APhP modes have larger wavevectors $q = 2\pi/\lambda_p$ and thus stronger confinement at the same frequency, though the other modes can also have deep subwavelength-scale confinement ($q \gg k_0$, k_0 being the wavevector in free space) at larger frequencies.

An important consequence of the large polariton wavevectors is the nonlocal responses induced in the materials.^{41,42} From acoustic graphene plasmons, it is known that there are two nonlocal effects: the nonlocal response of graphene and

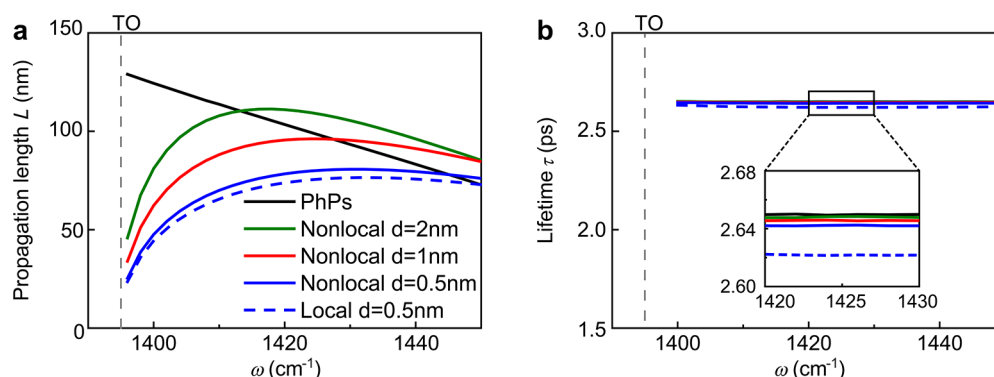


Figure 3. Propagation length L and lifetimes τ of hBN monolayer APhPs and PhPs. Propagation length (a) and lifetimes (b) of APhPs calculated for three different gap widths, $d = 2$ nm (solid green line), $d = 1$ nm (solid red line), $d = 0.5$ nm (solid blue line) for a nonlocal Au and of PhPs (solid black line). Dashed blue lines in (a) and (b) show the results of the APhPs for the hBN layer on the local Au ($d = 0.5$ nm), which are slightly different from the results obtained for nonlocal Au. The inset in (b) shows a zoom-in view to the four curves.

the nonlocal response of the metal substrate.⁴³ For our study of APhPs, we consider only the nonlocal effect in the metal substrate. As pointed out in ref 40, for 2D phononic materials, the nonlocal correction to the effective conductivity (permittivity) should be taken into account for the wavevector comparable to the inverse of the out-of-plane atomic layer spacing a (or that of in-plane lattice distance), $1/a > 20000k_0$. Such a large wavevector is challenging to be achieved by either PhPs or APhPs in the presence of practical material losses. Thus, the nonlocality in monolayer hBN can be neglected in our calculations. On the other hand, the large wavevector of APhPs can induce the nonlocal effects in the metal below the hBN layer, which has not been considered in the calculations shown in Figure 1. To elucidate the influence of nonlocal effects in the metal, we thus repeated the calculations of the APhP dispersion by considering a nonlocal response of the Au substrate (for details, see Methods) below a monolayer hBN (gap $d = 0.5$ nm). The results are plotted as solid blue line in Figure 2a. It is seen that accounting for the nonlocal Au substrate reduces the polariton wavevector and thus weakens the polariton confinement, which is in qualitative agreement with previous studies of acoustic graphene plasmons.⁴³ Note that the slight reduction of polariton wavevector resulting from nonlocal effect in Au substrate in our case is weaker than that of acoustic graphene plasmons that exhibit the nonlocalities from not only the metal underneath but also graphene.⁴³

Another distinguished advantage of APhPs over PhPs in the hBN monolayer is that the polariton confinement can be tuned by changing the gap width between the hBN and the nonlocal Au substrate. Figure 2a shows the calculated dispersions of APhPs for three different gap widths. It can be seen that the wavevector (and thus the confinement) of APhPs significantly increases with reducing gap widths d from 2 nm (solid green line) and 1 nm (solid red line) to 0.5 nm (solid blue line) at the same frequency. Our calculation also indicates that the APhP modes are sensitive to thickness changes of the spacer layer and thus to the roughness of the metal layer and the spacer layer itself. We thus suggest to use single crystalline gold platelets for an experimental demonstration, which are atomically flat and have been routinely used.^{44,45} Note that, in a practical experiment, the thickness of the spacer layer could be controlled with atomic-scale precision employing atomic layer deposition (ALD).²⁹ Further, a mono- or multilayer of another insulating vdW material could be used as the spacer layer. To better illustrate the thickness-tuning

effect, in Figure 2b we plot the APhP wavevector q as a function of d for a fixed frequency $\omega = 1400$ cm^{-1} (for the nonlocal Au below the hBN). As d increases from 0.5 nm to about 20 nm, one can observe a rapid decrease in the APhP wavevector (red line). This is because the coupling between the polaritons in monolayer hBN and the nonlocal Au substrate weakens when the polariton wavelength λ_p becomes comparable to the gap width d . When further increasing d to 60 nm, the APhP wavevector becomes nearly the same as that of PhPs ($q = 45k_0$, indicated by black dash line), indicating that the coupling between the polaritons and the Au substrate vanishes.

Based on the dispersions, the group velocities^{3,46} of APhPs for different d are calculated according to $V_g = \partial\omega/\partial q$ and are shown in Figure 2c. Remarkably, the APhPs are extremely slow polariton modes with group velocities $V_g \sim c/50000$ (c is the velocity of light in free space) at $d = 0.5$ nm near the TO (transverse optical phonon) frequency of hBN. This group velocity is much smaller than that of the PhPs in the hBN monolayer ($V_g \sim c/10000$), phonon polaritons with a type-II hyperbolic dispersion in thick hBN layer⁴⁷ ($V_g \sim c/500$) and acoustic graphene plasmons^{42,48} ($V_g \sim c/500$) at a given frequency. The extremely slow APhPs could be of fundamental importance for exploring strong light–matter interactions for applications such as polariton-enhanced vibrational sensing and enhanced nonlinear effects.

We also numerically calculate the propagation lengths of the APhPs by using $L = 1/\gamma$, as shown in Figure 3a. γ is the imaginary part of the polariton wavevector, which was calculated by the COMSOL mode solver. The propagation length L of APhPs decreases with reducing gap width d and shows a smaller value than that of PhPs near TO frequency, for example, $L_{\text{APhPs}} = 44$ nm at 1400 cm^{-1} for $d = 0.5$ nm and $L_{\text{PhPs}} = 124$ nm at 1400 cm^{-1} . To evaluate the polariton damping, as shown in Figure 3b, we directly calculate the polariton lifetime³ τ according to $\tau = L/2V_g$ by using the propagation lengths of Figure 3a and group velocities of Figure 2c. Interestingly, the lifetimes of PhPs (solid black line) and APhPs for different gap widths (solid green, solid red, and solid blue lines) are nearly the same (~ 2.6 ps) and almost constant with respect to frequency. Such results indicate that the losses of APhPs mainly result from the hBN layer, rather than from the Au substrate underneath. The Au substrate does not cause additional losses because of its large negative permittivity at mid-infrared frequencies (Au can be considered as a nearly

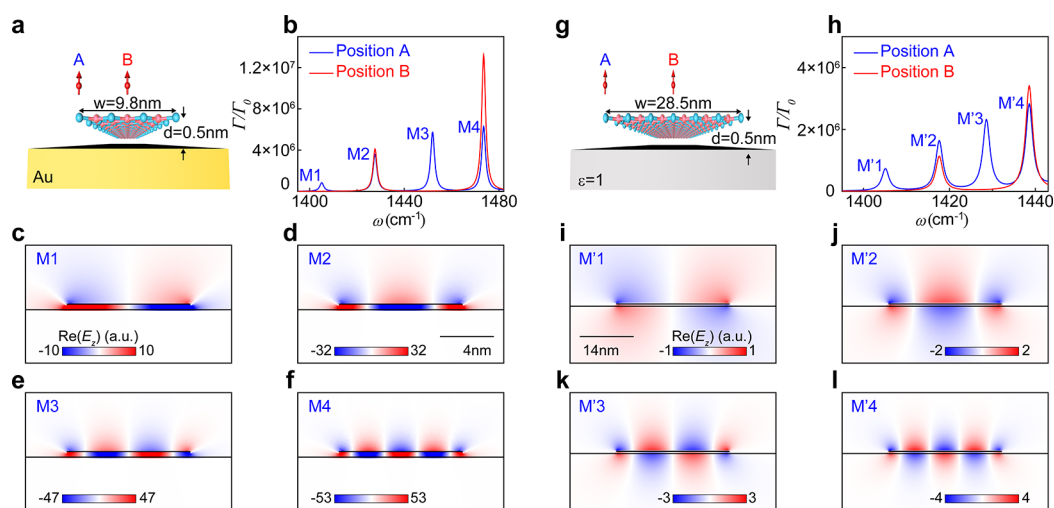


Figure 4. APhP and PhP ribbon nanoresonators. (a) Schematic of the APhP ribbon nanoresonator ($w = 9.8$ nm, $d = 0.5$ nm). (b) Normalized decay rates (Γ/Γ_0) of a dipole at positions A (0.5 nm above the hBN edge, blue line) and B (0.5 nm above the hBN center, red line) marked in (a). Γ and Γ_0 are the decay rates of the dipole in the resonator and in free space, respectively. (c–f) Electric field distribution $\text{Re}(E_z)$ of the resonating modes (M1–M4) in the APhP nanoresonator. (g) Schematic of the PhP ribbon nanoresonator ($w = 28.5$ nm, $d = 0.5$ nm). (h) Normalized decay rates (Γ/Γ_0) of a dipole at positions A (0.5 nm above the hBN edge) and B (0.5 nm above the hBN center) marked in (g). (i–l) Electric field distribution $\text{Re}(E_z)$ of the resonating modes in the PhP (M'1–M'4) nanoresonator. Note that we consider the nonlocal Au in the simulations.

perfect electric conductor). For that reason, field penetration into Au and subsequent damping of the polariton field in the substrate is negligible.

The combination of extreme confinement, ultraslow group velocities and long lifetimes makes APhPs an intriguing platform for polariton-enhanced infrared molecular sensing applications. We thus propose and numerically study the application potential of APhP-based nanoresonators for enhancing molecular vibrational fingerprints of extremely deep subwavelength scale amount of material. As sketched in Figure 4a, the resonator consists of a monolayer hBN ribbon on a nonlocal Au substrate with a separation gap (width $d = 0.5$ nm). In the simulations, we place a vertical electric dipole (as a point source) 0.5 nm above the nanoresonators to excite polariton resonances. Note that an ultrasharp metallic tip in the scattering-type scanning near-field optical microscopy (s-SNOM) could be used as the point source for exciting the APhP resonators in potential experiments.⁴⁹ For comparison, we also investigate the PhP counterpart (schematic in Figure 4g), which is a hBN monolayer placed above a transparent dielectric substrate ($\epsilon = 1$). To ensure that the fundamental resonances of both resonators occur at the given frequency of 1405 cm^{-1} , the width of the hBN layer is chosen to be 9.8 nm for the APhP resonator (Figure 4a) and 28.5 nm for the PhP resonator (Figure 4g), respectively. The dipole is located at two different lateral positions above the gap (A: the edge, B: the center, as shown in Figure 4a,g).

To evaluate the polariton resonances, we calculate the decay rate²⁷ of the dipole source in APhP resonators, $\Gamma = -\frac{2\pi}{c}\text{Re}[E_z(\mathbf{r}_0)]$. According to refs 27 and 50, the decay rate Γ characterizes the radiated power of the dipole, reflecting the electromagnetic interaction between the dipole and the resonator. $E_z(\mathbf{r}_0)$ is the z component of the electric field at the position of the dipole, which can be calculated by the full wave simulations. As shown in Figure 4b, the normalized decay rate Γ/Γ_0 (Γ_0 is the decay rate of the dipole source in free space) exhibits four peaks in the investigated frequency range when the dipole locates at the position A (blue line in Figure 4b).

These peaks correspond to the ribbon's polariton resonances with different orders (marked by M1–M4), whose electric field distributions are provided in Figure 4c–f. When the dipole is located at position B, the spectral decay rate (red line in Figure 4b) exhibits only two peaks that correspond to the even-order polariton resonances (i.e., M2 and M4) of the ribbons. The modal electric fields of the odd-order resonances exhibit nodes at the center of the ribbons and, thus, cannot be excited by the dipole²⁷ located at the position B. We also show the decay rates of the dipole in PhP resonators in Figure 4h and the electric field distributions of their resonances (denoted by M'1–M'4) in Figure 4i–l. We observe that the electric field $\text{Re}(E_z)$ maximum of the APhP resonance is over 1 order of magnitude larger than that of the PhP resonance, which can be attributed to the strong near-field enhancement inside the gap of the APhP resonator.

We further perform numerical simulations to study the performance of APhP resonators (monolayer hBN ribbon above nonlocal Au substrate) for enhancing molecular vibrational spectroscopy signals (Figure 5). Here we choose an organic molecule, CBP (4,4'-bis(*N*-carbazolyl)-1,1'-biphenyl), exhibiting an absorption peak at $\omega = 1450\text{ cm}^{-1}$, whose permittivity is plotted in Figure 5d. In the simulations, we place a vertical electric dipole at the height of 0.5 nm above the hBN ribbon to excite the APhPs (schematic in Figure 5a). The width of ribbon is adjusted as $w = 4.2$ nm to ensure that the APhPs can strongly couple with the CBP molecular vibration. We fill the gap with a dielectric reference (the permittivity $\epsilon = 3.1$) to ensure the APhP resonance at $\omega = 1450\text{ cm}^{-1}$. The simulated decay rate spectrum (Γ/Γ_0 , red line of Figure 5e) shows that the sharp M2 resonance peak indeed occurs at $\omega = 1450\text{ cm}^{-1}$ (electric field distribution shown in inset of Figure 5a). Its full-width-at-half-maximum (fwhm) of about 2.0 cm^{-1} corresponds to an ultrahigh quality factor $Q \sim 725$. For comparison, we also simulate the decay rate spectrum for the M'2 resonance (blue line of Figure 5e, peak at 1450 cm^{-1} , fwhm = 2.0 cm^{-1}) of the PhP resonator with $w = 6.8$ nm and a dielectric reference of $\epsilon = 3.1$ inside the 0.5 nm wide gap between monolayer hBN ribbon and $\epsilon = 1$ substrate

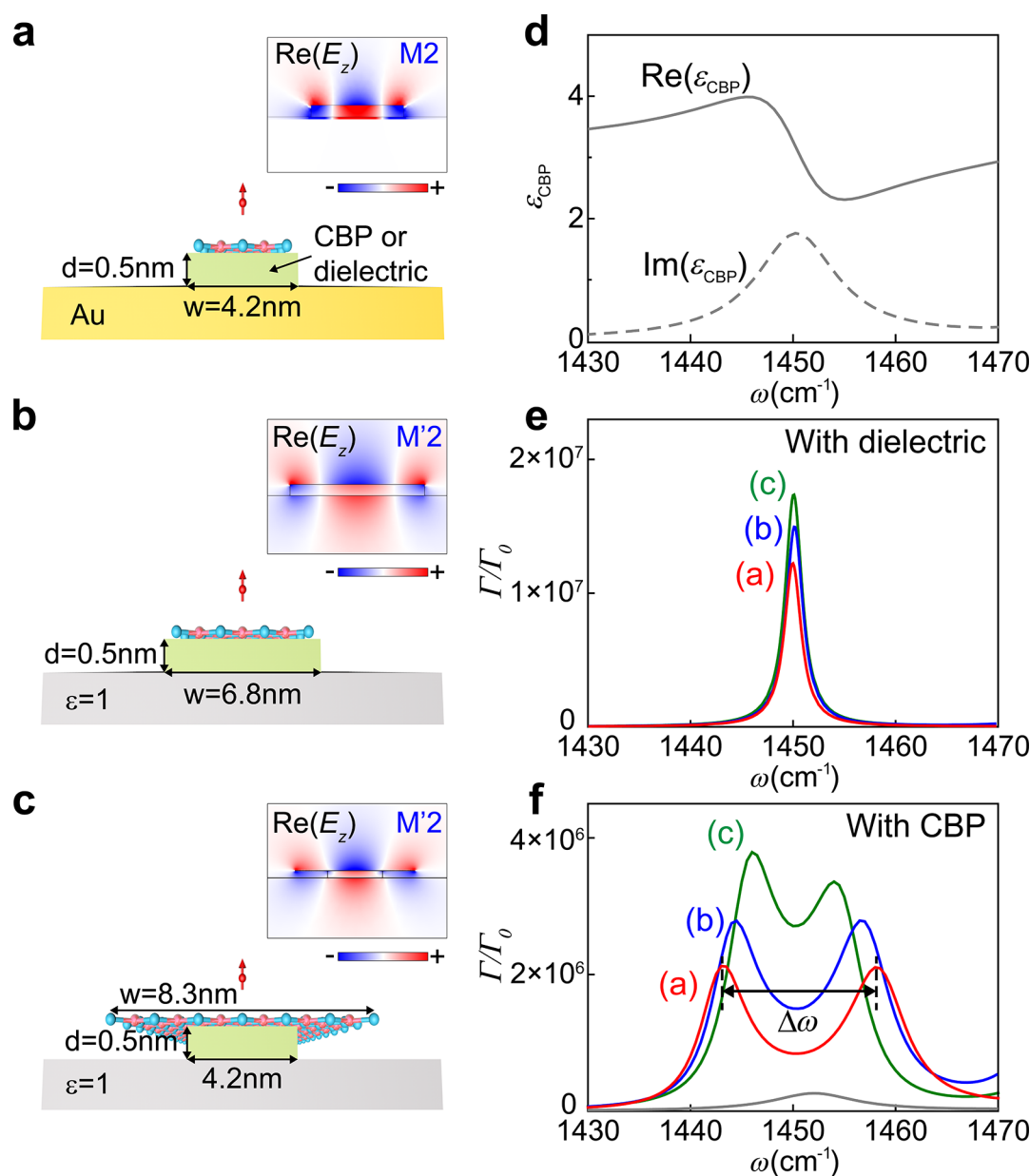


Figure 5. APhP ribbon nanoresonators for vibrational strong interactions and field-enhanced molecular spectroscopy. (a–c) Schematics of three different APhP and PhP nanoresonators (all the gaps are filled by dielectrics or CBP molecules). The inset in each figure shows the near-field distribution (the component $\text{Re}(E_z)$) of the resonators at resonance. The color scales for the three near-field profiles are the same. (a) APhP nanoresonator with $w = 4.2 \text{ nm}$ and $d = 0.5 \text{ nm}$. (b) PhP nanoresonator with $w = 6.8 \text{ nm}$ and $d = 0.5 \text{ nm}$. (c) PhP nanoresonator with $w = 8.3 \text{ nm}$ and $d = 0.5 \text{ nm}$, partly filled with the same amount of CBP molecules as the APhP resonator (4.2 nm in width). (d) Real part (solid line) and imaginary part (dashed line) of the permittivity of CBP molecules in the frequency range of interest. (e) Normalized decay rate (Γ/Γ_0) of a dipole placed 0.5 nm above the nanoresonators shown in (a)–(c) with the gap filled by the dielectric reference ($\epsilon = 3.1$). (f) Normalized decay rate (Γ/Γ_0) of a dipole placed 0.5 nm above the nanoresonators in (a)–(c) with CBP molecules inside the gaps. The gray line shows the result for CBP molecules in absence of APhP/PhP resonators. Note that we consider the nonlocal Au in the simulations.

(schematic in Figure 5b, w is chosen such that the PhPs can strongly couple with CBP vibration and dielectric reference is chosen to exhibit the PhP resonance at 1450 cm^{-1}). The same quality factors of M2 and M'2 modes indicate again that the Au substrate in the APhP resonator does not induce additional absorption. Moreover, we observe that the decay rate of the dipole above the APhP resonator is smaller than that in the PhP resonators. This is because the dipole source above the monolayer hBN less efficiently couples with the APhP fields, as the APhP fields are strongly confined inside the gap between the hBN and the Au substrate, and they decay very fast outside

the gap (analogously to acoustic plasmons in graphene^{29,30,51} and black phosphorus^{51,52}).

Strikingly, when the gap in APhP resonator is filled with CBP molecules, the decay rate spectrum is strongly modified by the CBP molecules and exhibits a strong peak splitting (red line in Figure 5f). The peak splitting ($\Delta\omega = 15.0 \text{ cm}^{-1}$) is larger than the sum of the fwhm of M2 mode (2.0 cm^{-1}) and the fwhm of the CBP absorption peak (10.0 cm^{-1} , determined from CBP spectrum, gray line of Figure 5f and in accord with CBP permittivity in Figure 5d), that is, $\Delta\omega = 15.0 \text{ cm}^{-1} > \text{fwhm}_{\text{M2}} + \text{fwhm}_{\text{CBP}} = 12.0 \text{ cm}^{-1}$, revealing strong coupling

between the APhP resonating mode and the CBP molecular vibrations.¹⁴ We also explore the PhP resonator when the gap is filled with CBP molecules. In this case, the peak splitting is only about 12.0 cm⁻¹ (blue line in Figure 5f), indicating a weaker coupling between the PhP mode and the CBP vibration than that in APhP resonator. Furthermore, as sketched in Figure 5c, we consider the case where the PhP resonator is filled with the same amount of CBP molecules as the APhP resonator (molecular layer width = 4.2 nm, height = 0.5 nm). Consequently, the peak splitting is further reduced to 8.0 cm⁻¹ (green line in Figure 5f), which is about 50% smaller than that of the APhP resonator. These results further indicate the remarkable capability of APhPs for sensing a very small amount of analyte molecules.

For an experimental demonstration of APhPs, the s-SNOM could be used to image them in real-space. The spatial resolution of s-SNOM is determined by the radius of the tip apex, which is typically around 20 nm. To excite and resolve the APhPs ($\lambda_p < 50$ nm), one could use an ultrasharp tip with an apex radius < 10 nm.⁵³ On the other hand, the signal-to-noise ratio (SNR) decreases for smaller tip radii, which could prevent reliable mapping. This problem may be tackled by using resonant antenna tips⁵⁴ comprising an ultrasharp tip apex, which could simultaneously improve both the SNR and the spatial resolution. Moreover, to fabricate APhP nano-resonators with ultracompressed mode volumes for infrared sensing, cavity quantum optics, and control of chemical interactions at a deeply subwavelength scale, one could deposit metal nanocubes onto monolayer hBN that is covered by a thin layer, analogously to experiments with acoustic graphene plasmons.⁵¹

In summary, we propose and theoretically demonstrate APhPs in monolayer-hBN/metal heterostructures. We show that the APhPs have larger confinement, stronger near-field enhancement, slower group velocities together with nearly the same polariton lifetimes compared to conventional PhPs in monolayer hBN. These properties make APhPs a promising candidate for exploring strong light-matter interactions at a deeply subwavelength scale. We also examine the nonlocal response of the metal substrate induced by the highly confined APhPs, which is equivalent to the effect of slightly increasing the width of gap between monolayer hBN and Au and thus weakens the electromagnetic confinement of the APhPs. We further demonstrate that APhP-based ribbon nano-resonators exhibit strong field confinement and large quality factors, which could be used to realize vibrational strong coupling between APhPs and molecular vibrations.

METHODS

Material Parameters Used in Simulations. The permittivity (in-plane $\epsilon_{\text{hBN},\perp}$; out-of-plane $\epsilon_{\text{hBN},\parallel}$) of the isotopically enriched h-BN used in this work is calculated according to a Lorentz model^{6,9}

$$\epsilon_{\text{hBN},j} = \epsilon_{\infty,j} \left(1 + \frac{\omega_{\text{LO},j}^2 - \omega_{\text{TO},j}^2}{\omega_{\text{TO},j}^2 - \omega^2 - i\omega\Gamma_j} \right)$$

Here, $j = \perp$ or \parallel indicates the direction perpendicular or parallel to the optical axis, $\omega_{\text{TO},j}$ and $\omega_{\text{LO},j}$ are the TO and LO phonon frequencies, Γ_j is the damping constant, and $\epsilon_{\infty,j}$ is the high-frequency permittivity. In this work, we take $\omega_{\text{TO},\parallel} = 785$ cm⁻¹, $\omega_{\text{LO},\parallel} = 845$ cm⁻¹, $\omega_{\text{TO},\perp} = 1395$ cm⁻¹, $\omega_{\text{LO},\perp} = 1630$ cm⁻¹, $\epsilon_{\infty,\parallel} = 2.8$, $\Gamma_{\parallel} = 1$ cm⁻¹, $\epsilon_{\infty,\perp} = 3$, and $\Gamma_{\perp} = 2$ cm⁻¹

according to ref 9. In simulations, the dielectric permittivity ϵ_{CBP} is modeled by three Lorentzians (identified by $k = 1-3$)

according to $\epsilon_{\text{CBP}} = \epsilon_{\infty} + \sum_k \frac{S_k^2}{\omega_k^2 - \omega^2 - i\omega\gamma_k}$. S_k^2 , ω_k^2 and γ_k

represent the intensity, central frequency, and damping of the k oscillator. For the vibration mode shown in Figure 5d, $k = 1$, $\epsilon_{\infty} = 2.8$, $\omega_1 = 1450$ cm⁻¹, and $\gamma_1 = 8.3$ cm⁻¹, respectively. The complete set of the permittivity function is listed in ref 14.

Modeling of a Nonlocal Metal Substrate. We model the nonlocal metal in our calculations by following the method described in ref 55. In this simple method, the spatial nonlocality of a metal can be represented by replacing the nonlocal metal with a composite material, comprising a thin dielectric layer on top of a local metal. The permittivity ϵ_d of that dielectric layer is given by the condition:⁵⁵

$$\frac{\epsilon_d}{\Delta} = \frac{\epsilon_b \epsilon_m q_L}{\epsilon_m - \epsilon_b}$$

where ϵ_m and ϵ_b are the permittivity of the local metal and the background, respectively. ϵ_m is described by a Drude model and $\epsilon_b = 1$. $q_L = \sqrt{q^2 + (\omega_p^2/\epsilon_{\infty} - \omega(\omega + i\gamma))/\beta^2}$ is the longitudinal polariton wavevector. ϵ_{∞} represents high-frequency permittivity of Au. γ and ω_p denote the electron damping and plasma frequency of Au. The β factor, representing the degree of nonlocality, is proportional to the Fermi velocity. Δ is the thickness of the dielectric layer, which should be chosen to be far smaller than the penetration depth in the metal. In our calculations, we choose $\epsilon_{\infty} = 1$, $\omega_p = 72500$ cm⁻¹, $\gamma = 216$ cm⁻¹, $\beta = 0.0036c$, and $\Delta = 0.1$ nm. As demonstrated in refs 43 and 55, this method works well for describing the nonlocal response in metals for both the analytic calculations and full-wave numerical simulations.

AUTHOR INFORMATION

Corresponding Authors

Peining Li – Wuhan National Laboratory for Optoelectronics and School of Optical and Electronic Information, Huazhong University of Science and Technology, Wuhan 430074, China; Email: lipn@hust.edu.cn

Xinliang Zhang – Wuhan National Laboratory for Optoelectronics and School of Optical and Electronic Information, Huazhong University of Science and Technology, Wuhan 430074, China; Email: xlzhang@hust.edu.cn

Authors

Zhu Yuan – Wuhan National Laboratory for Optoelectronics and School of Optical and Electronic Information, Huazhong University of Science and Technology, Wuhan 430074, China

Runkun Chen – Wuhan National Laboratory for Optoelectronics and School of Optical and Electronic Information, Huazhong University of Science and Technology, Wuhan 430074, China; orcid.org/0000-0003-3410-4863

Alexey Y. Nikitin – Donostia International Physics Center (DIPC), 20018 Donostia-San Sebastián, Spain; IKERBASQUE, Basque Foundation for Science, 48011 Bilbao, Spain; orcid.org/0000-0002-2327-0164

Rainer Hillenbrand – IKERBASQUE, Basque Foundation for Science, 48011 Bilbao, Spain; CIC NanoGUNE BRTA, Department of Electricity and Electronics, EHU/UPV, 20018 Donostia-San Sebastian, Spain; orcid.org/0000-0002-1904-4551

Complete contact information is available at:

<https://pubs.acs.org/10.1021/acsphotonics.0c00981>

Author Contributions

[†]These authors contributed equally to this work.

Notes

The authors declare no competing financial interest.

ACKNOWLEDGMENTS

We acknowledge the National Key Research and Development Project (Grant No. 2018YFA0704403). R.H. acknowledges financial support from the Spanish Ministry of Science, Innovation and Universities (National Project RTI2018-094830-B-I00 and the Project MDM-2016-0618 of the Marie de Maeztu Units of Excellence Program) and the Basque Government (Grant No. IT1164-19). A.Y.N. acknowledges the Spanish Ministry of Science, Innovation and Universities (National Project No. MAT2017-88358-C3-3-R). P.L. acknowledges the start-up funding from Huazhong University of Science and Technology.

REFERENCES

- (1) Caldwell, J. D.; Kretinin, A. V.; Chen, Y.; Giannini, V.; Fogler, M. M.; Francescato, Y.; Ellis, C. T.; Tischler, J. G.; Woods, C. R.; Giles, A. J.; Hong, M.; Watanabe, K.; Taniguchi, T.; Maier, S. A.; Novoselov, K. S. Sub-diffractive volume-confined polaritons in the natural hyperbolic material hexagonal boron nitride. *Nat. Commun.* **2014**, *5* (1), 5221–5221.
- (2) Li, P.; Yang, X.; Mas, T. W. W.; Hanss, J.; Lewin, M.; Michel, A. U.; Wuttig, M.; Taubner, T. Reversible optical switching of highly confined phonon-polaritons with an ultrathin phase-change material. *Nat. Mater.* **2016**, *15* (8), 870–875.
- (3) Yoxall, E.; Schnell, M.; Nikitin, A. Y.; Txoperena, O.; Woessner, A.; Lundberg, M. B.; Casanova, F.; Hueso, L. E.; Koppens, F. H. L.; Hillenbrand, R. Direct observation of ultraslow hyperbolic polariton propagation with negative phase velocity. *Nat. Photonics* **2015**, *9* (10), 674–678.
- (4) Tsakmakidis, K. L.; Hess, O.; Boyd, R. W.; Zhang, X. Ultraslow waves on the nanoscale. *Science* **2017**, *358* (6361), ea5196.
- (5) Dai, S.; Fei, Z.; Ma, Q.; Rodin, A. S.; Wagner, M.; McLeod, A. S.; Liu, M. K.; Gannett, W.; Regan, W.; Watanabe, K.; Taniguchi, T.; Thiemens, M.; Dominguez, G.; Neto, A. H. C.; Zettl, A.; Keilmann, F.; Jarillo-Herrero, P.; Fogler, M. M.; Basov, D. N. Tunable Phonon Polaritons in Atomically Thin van der Waals Crystals of Boron Nitride. *Science* **2014**, *343* (6175), 1125–1129.
- (6) Giles, A. J.; Dai, S.; Vurgaftman, I.; Hoffman, T.; Liu, S.; Lindsay, L.; Ellis, C. T.; Assefa, N.; Chatzakis, I.; Reinecke, T. L.; Tischler, J. G.; Fogler, M. M.; Edgar, J. H.; Basov, D. N.; Caldwell, J. D. Ultralow-loss polaritons in isotopically pure boron nitride. *Nat. Mater.* **2018**, *17* (2), 134–139.
- (7) Dai, S.; Ma, Q.; Andersen, T.; McLeod, A. S.; Fei, Z.; Liu, M. K.; Wagner, M.; Watanabe, K.; Taniguchi, T.; Thiemens, M.; Keilmann, F.; Jarillo-Herrero, P.; Fogler, M. M.; Basov, D. N. Subdiffractive focusing and guiding of polaritonic rays in a natural hyperbolic material. *Nat. Commun.* **2015**, *6* (1), 6963–6963.
- (8) Li, P.; Lewin, M.; Kretinin, A. V.; Caldwell, J. D.; Novoselov, K. S.; Taniguchi, T.; Watanabe, K.; Gaussmann, F.; Taubner, T. Hyperbolic phonon-polaritons in boron nitride for near-field optical imaging and focusing. *Nat. Commun.* **2015**, *6* (1), 7507–7507.
- (9) Li, P.; Dolado, I.; Alfaro-Mozaz, F. J.; Casanova, F.; Hueso, L. E.; Liu, S.; Edgar, J. H.; Nikitin, A. Y.; Velez, S.; Hillenbrand, R. Infrared hyperbolic metasurface based on nanostructured van der Waals materials. *Science* **2018**, *359* (6378), 892–896.
- (10) Ma, W.; Alonso-Gonzalez, P.; Li, S.; Nikitin, A. Y.; Yuan, J.; Martín-Sánchez, J.; Taboada-Gutiérrez, J.; Amenabar, I.; Li, P.; Velez, S.; Tolan, C.; Dai, Z.; Zhang, Y.; Sriram, S.; Kalantar-Zadeh, K.; Lee, S.-T.; Hillenbrand, R.; Bao, Q. In-plane anisotropic and ultra-low-loss polaritons in a natural van der Waals crystal. *Nature* **2018**, *562* (7728), 557–562.
- (11) Alfaro-Mozaz, F. J.; Alonso-Gonzalez, P.; Velez, S.; Dolado, I.; Autore, M.; Mastel, S.; Casanova, F.; Hueso, L. E.; Li, P.; Nikitin, A. Y.; Hillenbrand, R. Nanoimaging of resonating hyperbolic polaritons in linear boron nitride antennas. *Nat. Commun.* **2017**, *8* (1), 15624–15624.
- (12) Kim, S.; Froch, J. E.; Christian, J.; Straw, M.; Bishop, J.; Totonjian, D.; Watanabe, K.; Taniguchi, T.; Toth, M.; Aharonovich, I. Photonic crystal cavities from hexagonal boron nitride. *Nat. Commun.* **2018**, *9* (1), 2623.
- (13) Brar, V. W.; Jang, M. S.; Sherrott, M. C.; Kim, S.; Lopez, J. J.; Kim, L.; Choi, M.; Atwater, H. A. Hybrid Surface-Phonon-Plasmon Polariton Modes in Graphene/Monolayer h-BN Heterostructures. *Nano Lett.* **2014**, *14* (7), 3876–3880.
- (14) Autore, M.; Li, P.; Dolado, I.; Alfaro-Mozaz, F. J.; Esteban, R.; Atxabal, A.; Casanova, F.; Hueso, L. E.; Alonso-Gonzalez, P.; Aizpuru, J.; Nikitin, A. Y.; Velez, S.; Hillenbrand, R. Boron nitride nanoresonators for phonon-enhanced molecular vibrational spectroscopy at the strong coupling limit. *Light: Sci. Appl.* **2018**, *7* (4), 17172–17172.
- (15) Foteinopoulou, S.; Devarapu, G. C. R.; Subramania, G. S.; Krishna, S.; Wasserman, D. Phonon-polaritons: enabling powerful capabilities for infrared photonics. *Nanophotonics* **2019**, *8* (12), 2129–2175.
- (16) Dolado, I.; Alfaro-Mozaz, F. J.; Li, P.; Nikulina, E.; Bylinkin, A.; Liu, S.; Edgar, J. H.; Casanova, F.; Hueso, L. E.; Alonso-Gonzalez, P.; Velez, S.; Nikitin, A. Y.; Hillenbrand, R. Nanoscale Guiding of Infrared Light with Hyperbolic Volume and Surface Polaritons in van der Waals Material Ribbons. *Adv. Mater.* **2020**, *32* (9), 1906530.
- (17) Folland, T. G.; Fali, A.; White, S. T.; Matson, J. R.; Liu, S.; Aghamiri, N. A.; Edgar, J. H.; Haglund, R. F.; Abate, Y.; Caldwell, J. D. Reconfigurable infrared hyperbolic metasurfaces using phase change materials. *Nat. Commun.* **2018**, *9* (1), 4371.
- (18) Hu, G.; Ou, Q.; Si, G.; Wu, Y.; Wu, J.; Dai, Z.; Krasnok, A.; Mazon, Y.; Zhang, Q.; Bao, Q.; Qiu, C.-W.; Alù, A. Topological polaritons and photonic magic angles in twisted α -MoO₃ bilayers. *Nature* **2020**, *582* (7811), 209–213.
- (19) Chen, M.; Lin, X.; Dinh, T. H.; Zheng, Z.; Shen, J.; Ma, Q.; Chen, H.; Jarillo-Herrero, P.; Dai, S. Configurable phonon polaritons in twisted α -MoO₃. *Nat. Mater.* **2020**, na.
- (20) Duan, J.; Capote-Robayna, N.; Taboada-Gutiérrez, J.; Álvarez-Pérez, G.; Prieto, I.; Martín-Sánchez, J.; Nikitin, A. Y.; Alonso-González, P. Twisted Nano-Optics: Manipulating Light at the Nanoscale with Twisted Phonon Polaritonic Slabs. *Nano Lett.* **2020**, *20* (7), 5323–5329.
- (21) Shen, L.; Lin, X.; Shalaginov, M. Y.; Low, T.; Zhang, X.; Zhang, B.; Chen, H. Broadband enhancement of on-chip single-photon extraction via tilted hyperbolic metamaterials. *Appl. Phys. Rev.* **2020**, *7* (2), 021403.
- (22) Jacob, Z. Nanophotonics: Hyperbolic phonon-polaritons. *Nat. Mater.* **2014**, *13* (12), 1081–1083.
- (23) Novoselov, K. S.; Jiang, D.; Schedin, F.; Booth, T.; Khotkevich, V. V.; Morozov, S. V.; Geim, A. K. Two-dimensional atomic crystals. *Proc. Natl. Acad. Sci. U. S. A.* **2005**, *102* (30), 10451–10453.
- (24) Velický, M.; Toth, P. S.; Rakowski, A. M.; Rooney, A. P.; Kozikov, A.; Woods, C. R.; Mishchenko, A.; Fumagalli, L.; Yin, J.; Zolyomi, V.; Georgiou, T.; Haigh, S. J.; Novoselov, K. S.; Dryfe, R. A. W. Exfoliation of natural van der Waals heterostructures to a single unit cell thickness. *Nat. Commun.* **2017**, *8* (1), 14410.
- (25) Dai, S.; Fang, W.; Rivera, N.; Stehle, Y.; Jiang, B.-Y.; Shen, J.; Tay, R. Y.; Ciccariello, C. J.; Ma, Q.; Rodan-Legrain, D.; Jarillo-Herrero, P.; Teo, E. H. T.; Fogler, M. M.; Narang, P.; Kong, J.; Basov, D. N. Phonon Polaritons in Monolayers of Hexagonal Boron Nitride. *Adv. Mater.* **2019**, *31* (37), 1806603.
- (26) Alonso-Gonzalez, P.; Nikitin, A. Y.; Gao, Y.; Woessner, A.; Lundberg, M. B.; Principi, A.; Forcellini, N.; Yan, W.; Velez, S.; Huber, A. J.; Watanabe, K.; Taniguchi, T.; Casanova, F.; Hueso, L. E.; Polini, M.; Hone, J.; Koppens, F. H. L.; Hillenbrand, R. Acoustic

terahertz graphene plasmons revealed by photocurrent nanoscopy. *Nat. Nanotechnol.* **2017**, *12* (1), 31–35.

(27) Chen, S.; Autore, M.; Li, J.; Li, P.; Alonso-Gonzalez, P.; Yang, Z.; Martin-Moreno, L.; Hillenbrand, R.; Nikitin, A. Y. Acoustic Graphene Plasmon Nanoresonators for Field Enhanced Infrared Molecular Spectroscopy. *ACS Photonics* **2017**, *4* (12), 3089–3097.

(28) Principi, A.; Asgari, R.; Polini, M. Acoustic plasmons and composite hole-acoustic plasmon satellite bands in graphene on a metal gate. *Solid State Commun.* **2011**, *151* (21), 1627–1630.

(29) Lee, I. H.; Yoo, D.; Avouris, P.; Low, T.; Oh, S. H. Graphene acoustic plasmon resonator for ultrasensitive infrared spectroscopy. *Nat. Nanotechnol.* **2019**, *14* (4), 313–319.

(30) Voronin, K. V.; Aguirreche, U. A.; Hillenbrand, R.; Volkov, V. S.; Alonso-González, P.; Nikitin, A. Y. Nanofocusing of acoustic graphene plasmon polaritons for enhancing mid-infrared molecular fingerprints. *Nanophotonics* **2020**, *9* (7), 2089–2095.

(31) Gu, X.; Lin, I.-T.; Liu, J.-M. Extremely confined terahertz surface plasmon-polaritons in graphene-metal structures. *Appl. Phys. Lett.* **2013**, *103* (7), 071103.

(32) Pisarra, M.; Sindona, A.; Riccardi, P.; Silkin, V. M.; Pitarke, J. M. Acoustic plasmons in extrinsic free-standing graphene. *New J. Phys.* **2014**, *16* (8), 083003.

(33) Lee, I.-H.; He, M.; Zhang, X.; Luo, Y.; Liu, S.; Edgar, J. H.; Wang, K.; Avouris, P.; Low, T.; Caldwell, J. D.; Oh, S.-H. Image polaritons in boron nitride for extreme polariton confinement with low losses. *Nat. Commun.* **2020**, *11*, 3649.

(34) Feres, F. H.; Mayer, R. A.; Barcelos, I. D.; Freitas, R. O.; Maia, F. C. B. Acceleration of Subwavelength Polaritons by Engineering Dielectric-Metallic Substrates. *ACS Photonics* **2020**, *7*, 1396.

(35) Ambrosio, A.; Tamagnone, M.; Chaudhary, K.; Jauregui, L. A.; Kim, P.; Wilson, W. L.; Capasso, F. Selective excitation and imaging of ultraslow phonon polaritons in thin hexagonal boron nitride crystals. *Light: Sci. Appl.* **2018**, *7* (1), 27.

(36) Ciano, C.; Giliberti, V.; Ortolani, M.; Baldassarre, L. Observation of phonon-polaritons in thin flakes of hexagonal boron nitride on gold. *Appl. Phys. Lett.* **2018**, *112* (15), 153101.

(37) Duan, J.; Chen, R.; Li, J.; Jin, K.; Sun, Z.; Chen, J. Launching Phonon Polaritons by Natural Boron Nitride Wrinkles with Modifiable Dispersion by Dielectric Environments. *Adv. Mater.* **2017**, *29* (38), 1702494.

(38) Feres, F. H.; Barcelos, I. D.; Mayer, R. A.; dos Santos, T. M.; Freitas, R. O.; Raschke, M. B.; Bahamon, D. A.; Maia, F. C. B. Dipole modelling for a robust description of subdiffractive polariton waves. *Nanoscale* **2019**, *11* (44), 21218–21226.

(39) Serrano, J.; Bosak, A.; Arenal, R.; Krisch, M.; Watanabe, K.; Taniguchi, T.; Kanda, H.; Rubio, A.; Wirtz, L. Vibrational Properties of Hexagonal Boron Nitride: Inelastic X-Ray Scattering and Ab Initio Calculations. *Phys. Rev. Lett.* **2007**, *98* (9), 095503.

(40) Rivera, N.; Christensen, T. H.; Narang, P. Phonon Polaritons in Two-Dimensional Materials. *Nano Lett.* **2019**, *19* (4), 2653–2660.

(41) Gubbin, C. R.; De Liberato, S. Optical Nonlocality in Polar Dielectrics. *Phys. Rev. X* **2020**, *10* (2), 021027.

(42) Lundberg, M. B.; Gao, Y.; Asgari, R.; Tan, C.; Van Duppen, B.; Autore, M.; Alonso-González, P.; Woessner, A.; Watanabe, K.; Taniguchi, T.; Hillenbrand, R.; Hone, J.; Polini, M.; Koppens, F. H. L. Tuning quantum nonlocal effects in graphene plasmonics. *Science* **2017**, *357* (6347), 187–191.

(43) Alcaraz Iranzo, D.; Nanot, S.; Dias, E. J. C.; Epstein, I.; Peng, C.; Efetov, D. K.; Lundberg, M. B.; Parret, R.; Osmond, J.; Hong, J.-Y.; Kong, J.; Englund, D. R.; Peres, N. M. R.; Koppens, F. H. L. Probing the ultimate plasmon confinement limits with a van der Waals heterostructure. *Science* **2018**, *360* (6386), 291–295.

(44) Huang, J.-S.; Callegari, V.; Geisler, P.; Brünig, C.; Kern, J.; Prangma, J. C.; Wu, X.; Feichtner, T.; Ziegler, J.; Weinmann, P.; Kamp, M.; Forchel, A.; Biagioni, P.; Sennhauser, U.; Hecht, B. Atomically flat single-crystalline gold nanostructures for plasmonic nanocircuitry. *Nat. Commun.* **2010**, *1* (1), 150.

(45) Frank, B.; Kahl, P.; Podbiel, D.; Spektor, G.; Orenstein, M.; Fu, L.; Weiss, T.; Horn-von Hoegen, M.; Davis, T. J.; Meyer zu

Heringdorf, F.-J.; Giessen, H. Short-range surface plasmonics: Localized electron emission dynamics from a 60-nm spot on an atomically flat single-crystalline gold surface. *Sci. Adv.* **2017**, *3* (7), e1700721.

(46) Jiang, Y.; Lin, X.; Low, T.; Zhang, B.; Chen, H. Group-Velocity-Controlled and Gate-Tunable Directional Excitation of Polaritons in Graphene-Boron Nitride Heterostructures. *Laser & Photonics Reviews* **2018**, *12* (5), 1800049.

(47) Li, P.; Dolado, I.; Alfaro-Mozaz, F. J.; Nikitin, A. Y.; Casanova, F.; Hueso, L. E.; Velez, S.; Hillenbrand, R. Optical Nanoimaging of Hyperbolic Surface Polaritons at the Edges of van der Waals Materials. *Nano Lett.* **2017**, *17* (1), 228–235.

(48) Politano, A.; Marino, A. R.; Formoso, V.; Farias, D.; Miranda, R.; Chiarello, G. Evidence for acoustic-like plasmons on epitaxial graphene on Pt(111). *Phys. Rev. B: Condens. Matter Mater. Phys.* **2011**, *84* (3), 033401.

(49) Maissen, C.; Chen, S.; Nikulina, E.; Govyadinov, A.; Hillenbrand, R. Probes for Ultrasensitive THz Nanoscopy. *ACS Photonics* **2019**, *6* (5), 1279–1288.

(50) Huidobro, P. A.; Nikitin, A. Y.; Gonzalezballesterio, C.; Martin-Moreno, L.; Garcıaıdal, F. J. Superradiance mediated by graphene surface plasmons. *Phys. Rev. B: Condens. Matter Mater. Phys.* **2012**, *85* (15), 155438.

(51) Epstein, I.; Alcaraz, D.; Huang, Z.; Pusapati, V.-V.; Hugonin, J.-P.; Kumar, A.; Deputy, X. M.; Khodkov, T.; Rappoport, T. G.; Hong, J.-Y.; Peres, N. M. R.; Kong, J.; Smith, D. R.; Koppens, F. H. L. Far-field excitation of single graphene plasmon cavities with ultracompressed mode volumes. *Science* **2020**, *368* (6496), 1219–1223.

(52) Lee, I. H.; Martin-Moreno, L.; Mohr, D. A.; Khaliji, K.; Low, T.; Oh, S. H. Anisotropic Acoustic Plasmons in Black Phosphorus. *ACS Photonics* **2018**, *5* (6), 2208–2216.

(53) Mastel, S.; Govyadinov, A. A.; Maissen, C.; Chuvilin, A.; Berger, A.; Hillenbrand, R. Understanding the Image Contrast of Material Boundaries in IR Nanoscopy Reaching 5 nm Spatial Resolution. *ACS Photonics* **2018**, *5* (8), 3372–3378.

(54) Huth, F.; Chuvilin, A.; Schnell, M.; Amenabar, I.; Krutokhvostov, R.; Lopatin, S.; Hillenbrand, R. Resonant Antenna Probes for Tip-Enhanced Infrared Near-Field Microscopy. *Nano Lett.* **2013**, *13* (3), 1065–1072.

(55) Luo, Y.; Fernandez-Dominguez, A. I.; Wiener, A.; Maier, S. A.; Pendry, J. B. Surface plasmons and nonlocality: a simple model. *Phys. Rev. Lett.* **2013**, *111* (9), 093901.